

# Mechanism of CO<sub>2</sub> hydrogenation to formates by homogeneous Ru-PNP pincer catalyst: from a theoretical description to performance optimization†

Georgy A. Filonenko,<sup>ab</sup> Emiel J. M. Hensen<sup>ab</sup> and Evgeny A. Pidko<sup>\*ab</sup>Cite this: *Catal. Sci. Technol.*, 2014, 4, 3474

The reaction mechanism of CO<sub>2</sub> hydrogenation by pyridine-based Ru-PNP catalyst in the presence of DBU base promoter was studied by means of density functional theory calculations. Three alternative reaction channels promoted by the complexes potentially present under the reaction conditions, namely the dearomatized complex **2** and the products of cooperative CO<sub>2</sub> (**3**) and H<sub>2</sub> (**4**) addition, were analysed. It is shown that the bis-hydrido Ru-PNP complex **4** provides the unique lowest-energy reaction path involving a direct effectively barrierless hydrogenolysis of the polarized complex **5\***. The reaction rate in this case is controlled by the CO<sub>2</sub> activation by Ru-H that proceeds with a very low barrier of ca. 20 kJ mol<sup>-1</sup>. The catalytic reaction can be hampered by the formation of a stable formato-complex **5**. In this case, the rate is controlled by the H<sub>2</sub> insertion into the Ru-OCHO coordination bond, for which a barrier of 65 kJ mol<sup>-1</sup> is predicted. The DFT calculations suggest that the preference for the particular route can be controlled by varying the partial pressure of H<sub>2</sub> in the reaction mixture. Under H<sub>2</sub>-rich conditions, the former more facile catalytic path should be preferred. Dedicated kinetic experiments verify these theoretical predictions. The apparent activation energies measured at different H<sub>2</sub>/CO<sub>2</sub> molar ratios are in a perfect agreement with the calculated values. Ru-PNP is a highly active CO<sub>2</sub> hydrogenation catalyst allowing reaching turnover frequencies in the order of 10<sup>6</sup> h<sup>-1</sup> at elevated temperatures. Moreover, a minor temperature dependency of the reaction rate attainable in excess H<sub>2</sub> points to the possibility of efficient CO<sub>2</sub> hydrogenation at near-ambient temperatures.

Received 2nd May 2014,  
Accepted 31st May 2014

DOI: 10.1039/c4cy00568f

[www.rsc.org/catalysis](http://www.rsc.org/catalysis)

## Introduction

Utilization of CO<sub>2</sub> as a renewable C1 building block in chemical synthesis is recognized as a key strategy for developing more sustainable chemical technologies.<sup>1–4</sup> Considerable attention has been devoted to CO<sub>2</sub> coupling reactions for the production of cyclic carbonates or carboxylic acid derivatives.<sup>5–10</sup> Alternatively, CO<sub>2</sub> can be hydrogenated to C1 chemicals, such as formic acid (FA)<sup>11,12</sup> and, more challenging, methanol.<sup>13–15</sup> In addition to being important chemical intermediates, these compounds can be utilized as hydrogen storage agents as long as the reverse dehydrogenation reaction can be made to produce only carbon dioxide as the byproduct.<sup>16–20</sup> Fully reversible

processes for H<sub>2</sub> storage/release have so far only been demonstrated for the CO<sub>2</sub>/FA pair.<sup>18–24</sup>

The hydrogenation of carbon dioxide to formates has been the subject of many experimental and theoretical studies. The main focus has been on homogeneous catalysts, some of them with very high activity for the formation of formates and also their decomposition.<sup>25–29</sup> Most of the homogeneous systems make use of noble metals,<sup>30,31</sup> although a substantial progress has recently been made using first-row transition metal, namely, Fe<sup>32,33</sup> and Co,<sup>34</sup> complexes. Despite the apparent simplicity of the overall reaction, the mechanism of the catalytic CO<sub>2</sub> hydrogenation by homogeneous catalysts is still under debate. One of the first examples of an active catalyst for CO<sub>2</sub> hydrogenation under supercritical conditions, [Ru(H)<sub>2</sub>(PMe<sub>3</sub>)<sub>3</sub>],<sup>35</sup> has been studied computationally by Sakaki and co-workers.<sup>36,37</sup> The authors identified CO<sub>2</sub> insertion into the Ru-H bond as the rate determining step (RDS) under water free conditions, whilst the coordination of H<sub>2</sub> to Ru-formate species was shown to determine the reaction rate in the presence of water. A subsequent detailed investigation by Urakawa *et al.* revealed that CO<sub>2</sub> insertion is a facile

<sup>a</sup> *Inorganic Materials Chemistry, Department of Chemical Engineering, Eindhoven University of Technology, P.O. Box 513, 5600 MB Eindhoven, The Netherlands.*  
E-mail: e.a.pidko@tue.nl

<sup>b</sup> *Institute for Complex Molecular Systems, Eindhoven University of Technology, P.O. Box 513, 5600 MB Eindhoven, The Netherlands*

† Electronic supplementary information (ESI) available: Reaction free energy diagrams for catalysis by **4** in DMF, results of small-scale CO<sub>2</sub> hydrogenation experiments with **1**. See DOI: 10.1039/c4cy00568f



process, whereas the H<sub>2</sub> insertion in the Ru–formate complex represents the rate determining step for [Ru(dmpe)<sub>2</sub>H<sub>2</sub>]-catalysed CO<sub>2</sub> hydrogenation.<sup>38</sup> These findings were used to rationalize the increased activity at elevated H<sub>2</sub> partial pressure, which represented a major inconsistency with the earlier proposal on the RDS nature of the CO<sub>2</sub> insertion step.

Substantial progress in the catalytic CO<sub>2</sub> hydrogenation was made when Ir-PNP pincer complexes were introduced as catalysts by Nozaki<sup>39</sup> and co-workers in 2009. The presence of a non-innocent PNP pincer ligand, which can be directly involved in chemical transformations in the course of the catalytic reaction,<sup>40–42</sup> increases the complexity with respect to the mechanistic analysis. In the presence of a base, the PNP ligands can be deprotonated resulting in formation of a basic cooperative site on the side-arm of the dearomatized PNP\* ligand that can participate in substrate activation<sup>40,41</sup> (see Scheme 1 for a related reaction for Ru-PNP complex, 1 → 2). As a result, two alternative pathways were proposed for the hydrogenation of CO<sub>2</sub> over Ir-PNP,<sup>43</sup> the first of which involves the deprotonative ligand dearomatization as the key reaction step. The alternative mechanism involves the OH<sup>−</sup>-assisted hydrogen cleavage in the H<sub>2</sub> σ-complex, which regenerates the initial state of the catalyst, as the RDS. The latter mechanism was supported in a theoretical study by Yang<sup>44</sup> and Ahlquist<sup>45</sup> who found that the direct base-assisted H<sub>2</sub> cleavage was more favourable than pathways involving the ligand participation. A similar conclusion was drawn for iron- and cobalt-based PNP catalysts.

Recently, the application of ruthenium pincer catalysts in CO<sub>2</sub> hydrogenation has been described.<sup>46,47</sup> The corresponding ruthenium pincer complexes bearing pyridine-based PNN and PNP ligands are known to reversibly bind CO<sub>2</sub><sup>48,49</sup> via a metal–ligand cooperative mechanism (2 → 3, Scheme 1). The resulting products of [1,3]-CO<sub>2</sub> addition can contribute to the overall performance of these catalysts in the hydrogenation reaction. Huff and Sanford<sup>46</sup> reported that Ru-PNN pincer<sup>50</sup> catalyst can be used for hydrogenation of CO<sub>2</sub> to formates with a rate (turnover frequency, TOF) of 2200 h<sup>−1</sup>. A mechanism involving the dearomatization of the PNN ligand has been proposed. This proposal was confirmed in reactivity studies, employing KO<sup>t</sup>Bu to liberate HCOO<sup>−</sup> at the end of

the catalytic cycle. However, the possibility of ligand deprotonation with catalytically superior K<sub>2</sub>CO<sub>3</sub> base has not been confirmed yet.

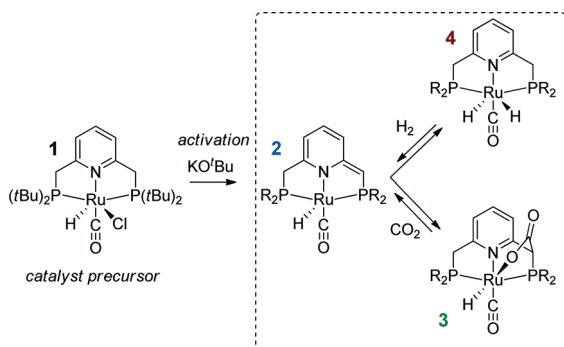
Previously, we have demonstrated that a related Ru-PNP catalyst 1 (ref. 50) (Scheme 1) shows remarkable catalytic performance in reversible CO<sub>2</sub> hydrogenation.<sup>22,47</sup> In a previous communication,<sup>47</sup> we investigated the mechanism of the catalytic reaction by a combination of kinetic experiments and *in situ* NMR experiments supported by DFT calculations. The results pointed to the inhibiting effect of the CO<sub>2</sub> adduct 3 on catalytic performance. In agreement with previous reports,<sup>38,43,44</sup> bis-hydrido Ru species were postulated as the active state. It was argued that the dearomatized Ru-PNP\* complex 2 did not contribute to the catalytic reaction. Nevertheless, the contribution of multiple reaction paths involving different species (Scheme 2) cannot be omitted and careful mechanistic analysis is required.

Herein, we present a systematic DFT study of the CO<sub>2</sub> hydrogenation to formates by Ru-PNP complexes that can be formed under reaction conditions. The catalytic cycles over the bis-hydrido complex 4, the dearomatized species 2 and the CO<sub>2</sub>-adduct 3 were considered (Scheme 2). This work is a continuation of our previous mechanistic study.<sup>47</sup> The main focus will be on the analysis of the reaction networks underlying the catalytic process to identify the catalytic role of different intermediates present in the reaction mixture. The theoretical insights are validated by dedicated experiments.

## Computational and experimental details

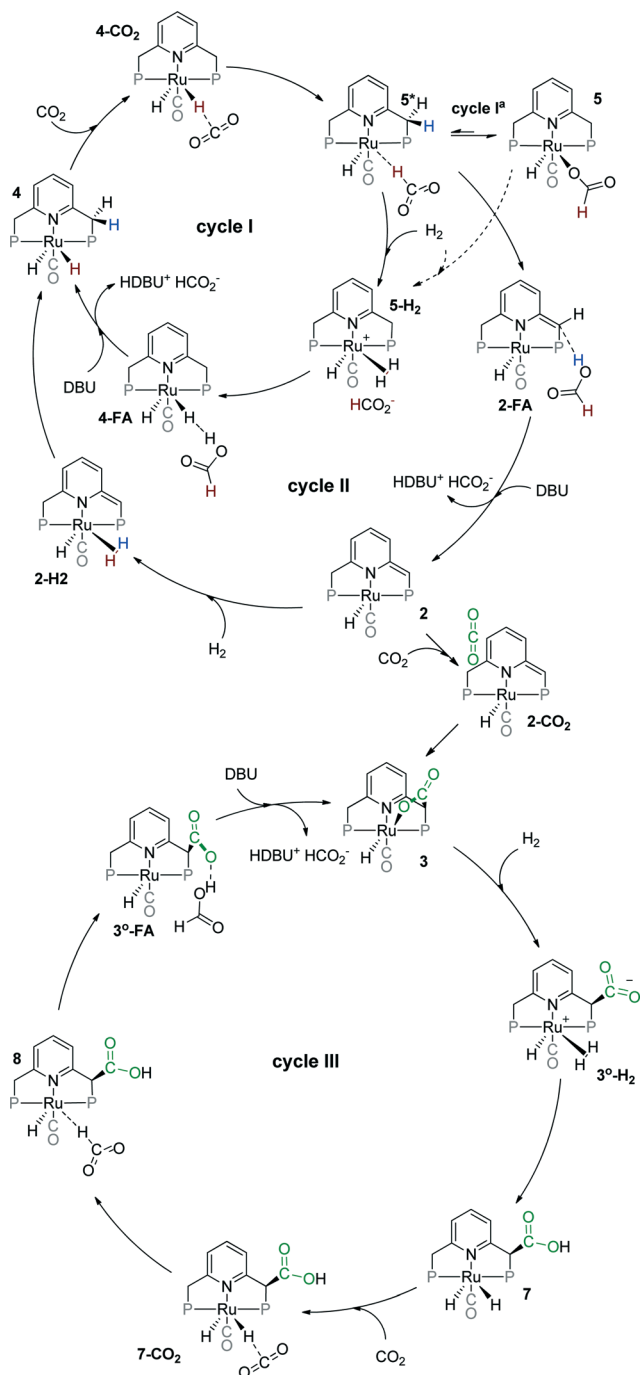
### Density functional theory calculations

Similar to our previous work,<sup>47</sup> density functional theory (DFT) calculations were performed with the PBE0 (also denoted as PBE1PBE and PBEh)<sup>51</sup> hybrid exchange–correlation functional using Gaussian 09, revision D.01 program.<sup>52</sup> The high accuracy of this method has been demonstrated by previous benchmark studies on a wide set of different chemical systems<sup>53,54</sup> and by our own accuracy tests employing different DFT methods for modelling CO<sub>2</sub> hydrogenation to formic acid.<sup>47</sup> The full electron 6-311G(d,p) basis set<sup>55,56</sup> was used for all atoms except ruthenium, for which the LanL2DZ basis set<sup>57,58</sup> was employed. The polarisable continuum model (PCM) with standard parameters for THF and DMF solvents, as implemented in the Gaussian 09 rev. D.01 program package, was used during the geometry optimization and frequency analysis to account for bulk solvent effects. Because the differences in reaction free energies computed with PCM model of THF and DMF solvents do not exceed 5 kJ mol<sup>−1</sup> (see ESI<sup>†</sup>), only the results obtained for the THF solvent are discussed here. The accuracy of this computational method was tested by calculating energetics of selected elementary reaction steps (2 + H<sub>2</sub> → 4 (ref. 47) and 4 + CO<sub>2</sub> → 5\*, Scheme 1) using a larger triple-zeta + polarization quality basis set combination employing Def2-TZVPP<sup>59</sup> basis set for the Ru centre and 6-311+G(d,p) for the light atoms. The resulting reaction and activation energies agreed



**Scheme 1** Activation of a Ru-PNP precursor 1 by deprotonation with a strong base and the subsequent metal–ligand cooperative activation of CO<sub>2</sub> and H<sub>2</sub>.





**Scheme 2** Possible catalytic cycles for CO<sub>2</sub> hydrogenation to formates by Ru-PNP pincer complexes (<sup>t</sup>Bu substituents of the ligand are omitted for clarity).

within 5 kJ mol<sup>-1</sup> with those obtained using the standard methodology (see ESI† and ref. 47). Note that the expansion of the basis set with diffuse functions has a negligible effect on the computed energetics, while it resulted in a much slower SCF convergence (when PCM model was used to account for solvent effects).

The nature of the stationary points was evaluated from the analytically computed harmonic modes. No imaginary

frequencies were found for the optimized structures, confirming that these correspond to local minima on the potential energy surface. All transition states exhibited a single imaginary frequency, corresponding to the eigenvector along the reaction path. The assignment of the transition state structure to a particular reaction path was tested by perturbing the structure along the reaction path eigenvector in the directions of the product and the reagent followed by geometry optimization. For catalytic cycles I, II and III starting from the activated species 3°-H<sub>2</sub> IRC calculations were performed to additionally confirm the assignment of the transition states. The reaction ( $\Delta E$ ) and activation energies ( $E^\ddagger$ ) reported in the manuscript were corrected for zero point ( $E_{ZPE}$ ) energy contribution computed using the results of the normal-mode analysis. Free energy values ( $\Delta G^\circ$ ) were computed using the results of the normal-mode analysis within the ideal gas approximation at a pressure of 1 atm and temperatures of 298 K.

### Catalytic CO<sub>2</sub> hydrogenation

All manipulations unless otherwise stated were performed using Schlenk techniques. Argon was dried with a Sicapent column. Air sensitive compounds were stored in a MBraun glovebox under an atmosphere of dry nitrogen or argon. Solvents were dispensed from MBraun solvent purification system. 1,8-Diazabicyclo[5.4.0]undec-7-ene (DBU) was purchased from Fluorochem and vacuum distilled from calcium hydride. Catalyst 1 was prepared according to original literature procedure.<sup>60</sup>

Small scale CO<sub>2</sub> hydrogenation experiments were performed in A96 parallel reactor at 70 °C under 40 bar of equimolar H<sub>2</sub>-CO<sub>2</sub> mixture. In a typical experiment 3 mL THF or DMF, and appropriate amount of base DBU (3.3 mmol) or KO<sup>t</sup>Bu (0.33 mmol) were mixed with 0.1 μmol of catalyst. The reaction was quenched after 2 hours by addition of water-ethanol mixture and immediately analyzed. Concentrations of formic acid were analyzed using Shimatzu HPLC setup with 25 mM phosphate buffer of pH = 2 as mobile phase using Prevail Organic Acid column. GC measurements, where appropriate, were performed using Shimatzu GC-17A instrument.

Kinetic measurements were carried out in Top Industrie 100 mL stainless steel autoclave. The vessel was evacuated overnight at 150 °C, purged several times with Ar, and the reaction medium was introduced by cannulae transfer. The autoclave was flushed with H<sub>2</sub>-CO<sub>2</sub> mixture or hydrogen, preheated to reaction temperature and filled with H<sub>2</sub>-CO<sub>2</sub> mixture up to operating pressure of 40 bar. The catalyst was then introduced *via* a dosage device and the reaction started. Constant pressure was maintained by a compensation device fitted with Bronkhorst EL-FLOW MFC unit and digital pressure meter with equimolar H<sub>2</sub>-CO<sub>2</sub> mixture. Samples were withdrawn *via* dip-tube installation (dead volume 4 μL, sampling volume 110 μL), diluted to 1 mL and immediately analysed by HPLC and GC-FID. In a typical experiment 30 mL solvent, 5 mL DBU (33.4 mmol), 1 mL toluene or THF (used



as an internal standard) and appropriate amount of catalysts dispensed from the stock solution were used. The kinetic traces represent single run results.

## Results and discussion

### Catalyst activation

Hydrogenation activity of Ru-PNP pincer is usually initiated by reacting a catalyst precursor **1** with a strong base to form a dearomatized Ru-PNP\* species **2** (Scheme 1). Both substrates of the catalytic CO<sub>2</sub> hydrogenation reaction, namely, CO<sub>2</sub> and H<sub>2</sub> can then undergo a metal–ligand cooperative addition to **2** resulting in rearomatized Ru-PNP complexes **3**<sup>49</sup> and **4**,<sup>50,61</sup> respectively. Fig. 1 shows the optimized structures of the involved reaction intermediates and transition states together with the computed energetics of the elementary reaction steps.<sup>47</sup> The reaction starts with the formation of molecular complexes of **2** with the substrate molecules. Despite very similar thermodynamics of complexation with CO<sub>2</sub> and H<sub>2</sub>, the nature of the formed species is quite different. Whereas no specific interaction between CO<sub>2</sub> and Ru-PNP\* is observed in 2–CO<sub>2</sub>, 2–H<sub>2</sub> represents a classical example of a σ-H<sub>2</sub> complex<sup>62–66</sup> featuring a highly symmetric η<sup>2</sup>-coordination of dihydrogen with short Ru–H distances and a considerably elongated H–H bond (*r*(H–H) = 0.821 Å vs. 0.747 Å for the free molecule).

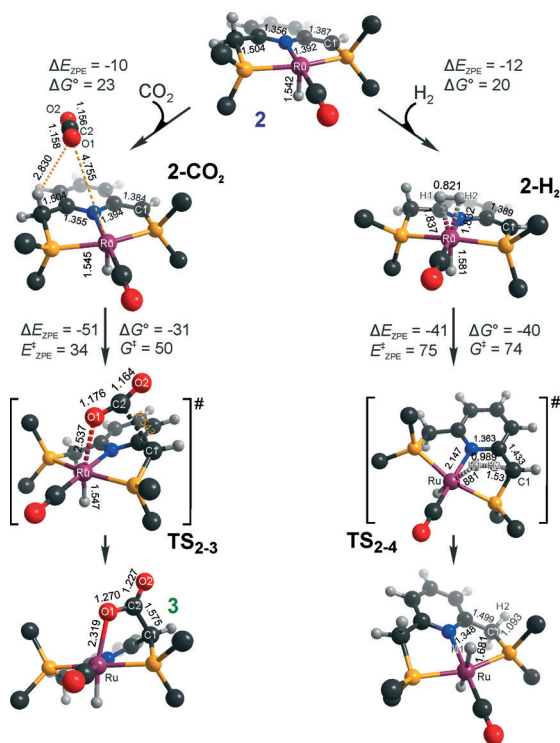


**Fig. 1** Optimized structures of reaction intermediates and transition states involved in the metal–ligand cooperative activation of H<sub>2</sub> and CO<sub>2</sub> by **2** (in the graphical representation <sup>t</sup>Bu substituents at the phosphine moieties are simplified for clarity). ZPE-corrected reaction ( $\Delta E_{ZPE}^{\ddagger}$ ) and activation energies ( $E_{ZPE}^{\ddagger}$ ), reaction and activation Gibbs free energies ( $\Delta G^{\circ}$  and  $G^{\ddagger}$ ) are given in kJ mol<sup>-1</sup> (for individual elementary steps).<sup>47</sup>

The cooperative [1,3]-addition of CO<sub>2</sub> (2–CO<sub>2</sub> → TS<sub>2-3</sub> → 3) is exothermic by –51 kJ mol<sup>-1</sup> and proceeds with a low activation barrier of 34 kJ mol<sup>-1</sup>. When corrected for entropic effects, the reaction and activation Gibbs free energies are, respectively, equal to –31 and 50 kJ mol<sup>-1</sup>. This evidences a pronounced entropy loss due to the decrease in the degrees of freedom upon the chemical binding of the non-specifically coordinated CO<sub>2</sub>. The TS<sub>2-3</sub> is an early transition state that features a distorted CO<sub>2</sub> molecule that forms rather elongated bonds with the basic C1 site of the ligand (*r*(C1–C2) = 2.543 Å) and the Ru center (*r*(Ru–O1) = 2.537 Å). The structural properties of TS<sub>2-3</sub> suggest that the dominant destabilizing contribution to the activation energy in this case is associated with the bending of the linear CO<sub>2</sub> molecule necessary for the attack by the basic C1 centre at the PNP\* pincer arm. The promoting effect of the concomitant coordination to Ru is the polarization of the CO<sub>2</sub> molecule and stabilization of the negative charge at the O1 atom (Mulliken atomic charge in TS<sub>2-3</sub> is –0.280 e<sup>-</sup>) in the course of the [1,3]-addition reaction towards **3**. The optimized structure of **3** agrees well with the single-crystal X-ray diffraction data reported by Milstein and co-workers.<sup>49</sup> The accuracy of the current computational method is supported by a good match between the calculated  $E^{\ddagger}$  and  $G^{\ddagger}$  (85 and 81 kJ mol<sup>-1</sup>, respectively) and the experimental values (94 and 83 kJ mol<sup>-1</sup>)<sup>49</sup> determined for the reverse 3 → 2 + CO<sub>2</sub> transformation.

Dissociation of H<sub>2</sub> over **2** gives a bis-hydrido Ru-PNP complex **4** (2–H<sub>2</sub> → TS<sub>2-4</sub> → 4, Fig. 1) and proceeds with an activation barrier ( $E_{ZPE}^{\ddagger} = 75$  kJ mol<sup>-1</sup>) substantially higher than that computed for the reaction with CO<sub>2</sub>. Because H<sub>2</sub> is effectively immobilized within the σ-complex 2–H<sub>2</sub>, the entropic contribution to the reaction and activation energy in this case is negligible. As a result the overall reaction 2 + H<sub>2</sub> → 4 ( $\Delta G^{\circ} = -40$  kJ mol<sup>-1</sup>) is more thermodynamically favourable than the reaction with CO<sub>2</sub> (2 + CO<sub>2</sub> → 3,  $\Delta G^{\circ} = -8$  kJ mol<sup>-1</sup>). In the TS<sub>2-4</sub>, the polarized H<sub>2</sub> molecule undergoes a heterolytic cleavage over a Ru⋯C1 acid–base pair. The calculated Mulliken charges on the H1 and H2 atoms in TS<sub>2-4</sub> are –0.056 and 0.187 e<sup>-</sup>, respectively. The high activation barrier in this case is most likely due to the relatively large distance between the acid and the base sites in the dearomatized Ru-PNP\* (**2**: *r*(C1⋯Ru) = 3.191 Å) that hampers the efficient stabilization of both the H<sup>-</sup> and H<sup>+</sup> species formed in the transition state.

An insight into the origin of the different coordination behaviour and reactivity of **2** towards CO<sub>2</sub> and H<sub>2</sub> can be obtained from the frontier orbital analysis (Fig. 3). An unoccupied d<sub>z2</sub> orbital on Ru and an occupied formally p<sub>z</sub> orbital on basic C1 contribute mostly to the LUMO and HOMO of **2**. HOMO-1 is dominated by an occupied Ru d<sub>yz</sub> orbital. These molecular orbitals (MOs) cannot form a positive overlap with the π\* LUMO and n HOMO orbitals of linear non-perturbed CO<sub>2</sub>. Their linear combination leads to a non-bonding interaction. This explains the non-specific coordination of carbon dioxide in 2–CO<sub>2</sub>. The change of hybridization of the C atom in CO<sub>2</sub> upon bending (CO<sub>2</sub><sup>\*</sup>) make a positive orbital overlap



between LUMO of  $\text{CO}_2^*$  and HOMO of **2** possible. The relatively small energy gap between these orbitals enhances the acid–base interaction resulting in a very low barrier of the [1,3]-addition of  $\text{CO}_2$  to **2**.

HOMO  $\sigma$  and LUMO  $\sigma^*$  orbitals of  $\text{H}_2$  can be involved in donation and back-donation interactions with LUMO and HOMO – 1 orbitals of **2**, respectively, in  $2\text{-H}_2$   $\sigma$ -complex. However, because of the large energy difference between the interacting orbitals, binding within the molecular complex is weak (Fig. 1). The specific coordination of  $\text{H}_2$  to **2** promotes the formation of **4**. In support of the above proposition, the high energy barrier for  $\text{H}_2$  dissociation is due to the distant location of the base site. Indeed, the complexation with  $\text{H}_2$  does not change the properties of the HOMO.

These results suggest that the preference towards the formation of complexes **3** and **4** during the catalytic  $\text{CO}_2$  hydrogenation can be altered by varying the reaction conditions. Indeed, whereas the reaction of **2** with  $\text{H}_2$  to the bis-hydrido complex **4** is more thermodynamically favourable, the alternative path towards the  $\text{CO}_2$  adduct **3** proceeds with a much lower activation barrier. This implies that by increasing partial pressure of  $\text{H}_2$  in the reaction mixture, the formation of **4** can be promoted. However, in the presence of excess base necessary to promote catalytic  $\text{CO}_2$  hydrogenation, one cannot exclude the transient formation of the dearomatized species **2**, which can also contribute to the catalytic activity of the Ru-PNP catalyst. To understand the behaviour of this system, analysis of reaction paths over these three alternative potentially active species is necessary.

### $\text{CO}_2$ hydrogenation over **4**

The calculated reaction energy diagram for the catalytic cycle I (Scheme 2) of  $\text{CO}_2$  hydrogenation by bis-hydrido Ru-PNP complex **4**<sup>47</sup> is shown in Fig. 3. The starting point of the reaction is an energy-neutral binding of  $\text{CO}_2$  to **4** resulting in  $4\text{-CO}_2$ . Weak intermolecular contacts between the O atoms of  $\text{CO}_2$  and acidic  $\text{CH}_2$  protons of the PNP pincer arms in  $4\text{-CO}_2$  ( $r(\text{O}\cdots\text{H}) = 2.584 \text{ \AA}$ ) direct the  $\text{CO}_2$  coordination towards the Ru–H moiety. This allows a facile attack of  $\text{CO}_2$  by Ru-bound hydride (Mulliken charge on the Ru-bound H atom is  $-0.152 e^-$ ) resulting in a formate anion ( $4\text{-CO}_2 \rightarrow \text{TS}_{4-5} \rightarrow 5^*$ ). The reaction is exothermic by  $-13 \text{ kJ mol}^{-1}$  and shows a very low activation barrier of  $23 \text{ kJ mol}^{-1}$ . Similar to [1,3]- $\text{CO}_2$  addition to **2**, the reaction is triggered by the increased acidity of the  $\text{sp}^2$ -like C atom in bent  $\text{CO}_2$  moiety formed in  $\text{TS}_{4-5}$  that ensures an efficient overlap between the s orbital of the  $\text{H}^-$  ligand being one of the main contributors of HOMO (**4**) (Fig. 4) and LUMO of  $\text{CO}_2^*$  (Fig. 2). Note that HOMO in complex **4** lies 1 eV lower than that in **2** indicating a lower nucleophilicity of the  $\text{H}^-$  ligand compared to the basic C1 centre in complexes **4** and **2**, respectively. This is in line with the much higher exothermicity of the cooperative  $\text{CO}_2$  activation by **2**.

At the next step Ru $\cdots$ H-coordinated  $\text{HCOO}^-$  anion is replaced by  $\text{H}_2$  yielding a cationic  $\sigma\text{-H}_2$  Ru-PNP complex

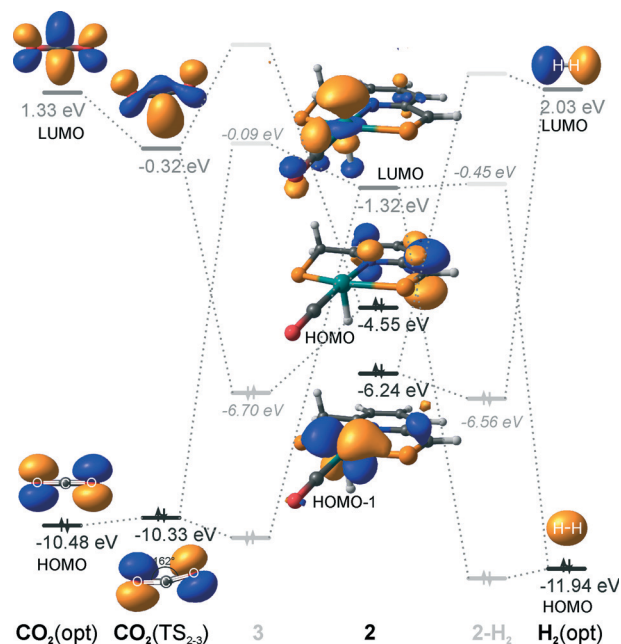


Fig. 2 Frontier orbitals of the dearomatized complex **2** optimized  $\text{H}_2$  and  $\text{CO}_2$  molecules ( $\text{H}_2(\text{opt})$  and  $\text{CO}_2(\text{opt})$ ) as well as those of the bent  $\text{CO}_2$  moiety from the  $\text{TS}_{2-3}$  structure ( $\text{CO}_2(\text{TS}_{2-3})$ ). <sup>t</sup>Bu at the phosphine moieties in **2** are omitted for clarity, while the respective MO contributions are visualized. Dotted lines depict possible orbital interactions following simplified symmetry considerations and solid grey lines represent the qualitative energetics of the resulting MOs in complexes **3** and  $2\text{-H}_2$  with the energy values indicated for the orbitals, for which the contribution of the interacting molecular fragments could be unambiguously defined.

charge-compensated by  $\text{HCOO}^-$  hydrogen bonded with the  $\text{CH}_2$  moieties of the ligand ( $5^* + \text{H}_2 \rightarrow 5\text{-H}_2$ ). Subsequent heterolytic dissociation of  $\text{H}_2$  over an acid–base pair composed of the Ru centre and the adjacent formate anion results in a molecular complex of formic acid with **4** ( $4\text{-FA}$ ). Despite a lower nucleophilicity of the  $\text{HCOO}^-$  moiety ( $E_{\text{HOMO}(5^{**})} = -6.10 \text{ eV}$ , Fig. 5) compared to the C1 site in **2** ( $E_{\text{HOMO}(2)} = -4.55 \text{ eV}$ , Fig. 3), the direct availability of a proton-accepting species in the immediate vicinity of the dissociating  $\text{H}_2$  molecule leads to a less strained  $\text{TS}_{5-4}$  transition state structure and, accordingly, to an extremely low activation barrier for the reaction. Indeed, the reactive moiety Ru $\cdots$ H–H in  $\text{TS}_{5-4}$  is characterized by substantially shorter interatomic distances ( $r(\text{Ru}\cdots\text{H}) = 1.785 \text{ \AA}$  and  $r(\text{H}\cdots\text{H}) = 0.920 \text{ \AA}$ , Fig. 3) compared to the respective parameters in  $\text{TS}_{2-4}$  ( $r(\text{Ru}\cdots\text{H}) = 1.881 \text{ \AA}$  and  $r(\text{H}\cdots\text{H}) = 0.989 \text{ \AA}$ , Fig. 3). Reaction of  $4\text{-FA}$  with the DBU base at the next step releases DBU–FA product and regenerates the initial complex **4**.

Alternatively,  $5^*$  can rearrange to a stable complex **5** (ref. 67) ( $5^* \rightarrow 5$ ,  $\Delta E_{\text{ZPE}} = -39 \text{ kJ mol}^{-1}$ , Fig. 3) featuring a direct Ru–O coordination ( $r(\text{Ru–O}) = 2.261 \text{ \AA}$ ). Previously, this species has been proposed to be a resting state in the catalytic cycle by **4**.<sup>47</sup> To proceed with the catalytic cycle (path I<sup>a</sup>), the ionization of **5** (*i.e.* the formation of an ion pair  $5^*$ ) and the replacement of  $\text{HCOO}^-$  with  $\text{H}_2$  has to take place. This reaction shows an activation barrier of  $65 \text{ kJ mol}^{-1}$ .



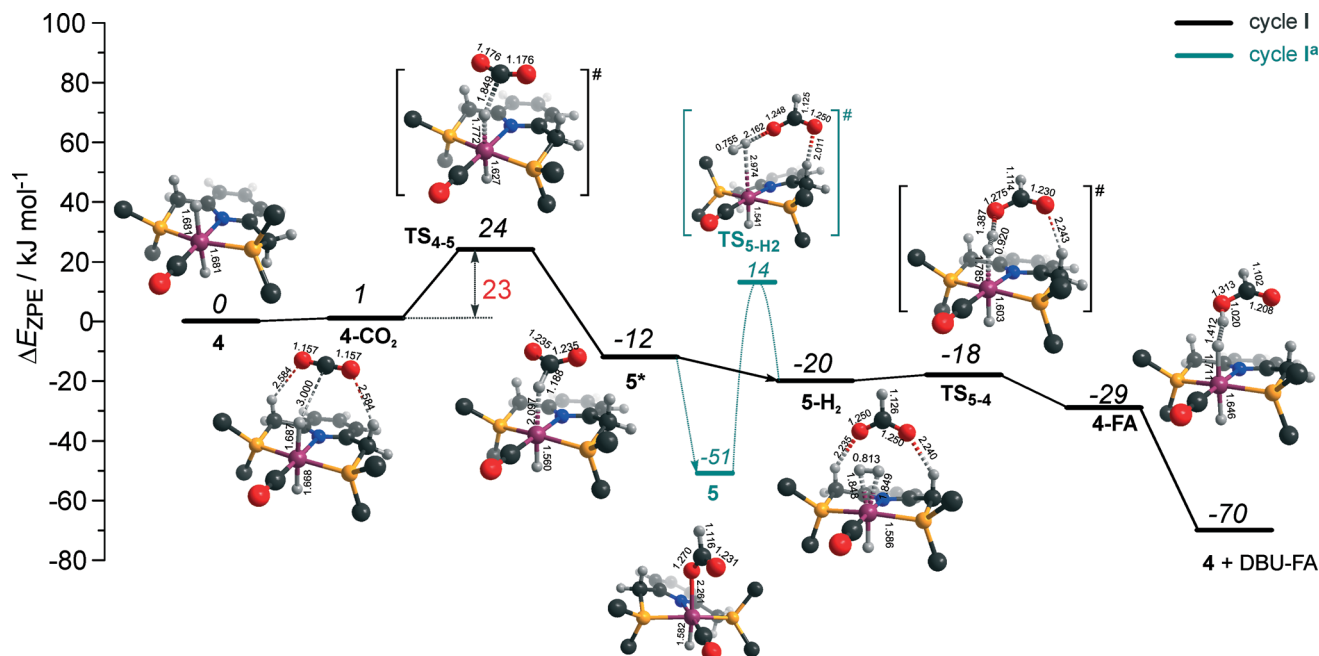


Fig. 3 DFT computed reaction energy diagram and optimized structures of the intermediate and transition states (CH<sub>3</sub> groups at the <sup>4</sup>Bu substituents of the PNP ligand are omitted for clarity) for the hydrogenation of CO<sub>2</sub> over **4**.<sup>47</sup>

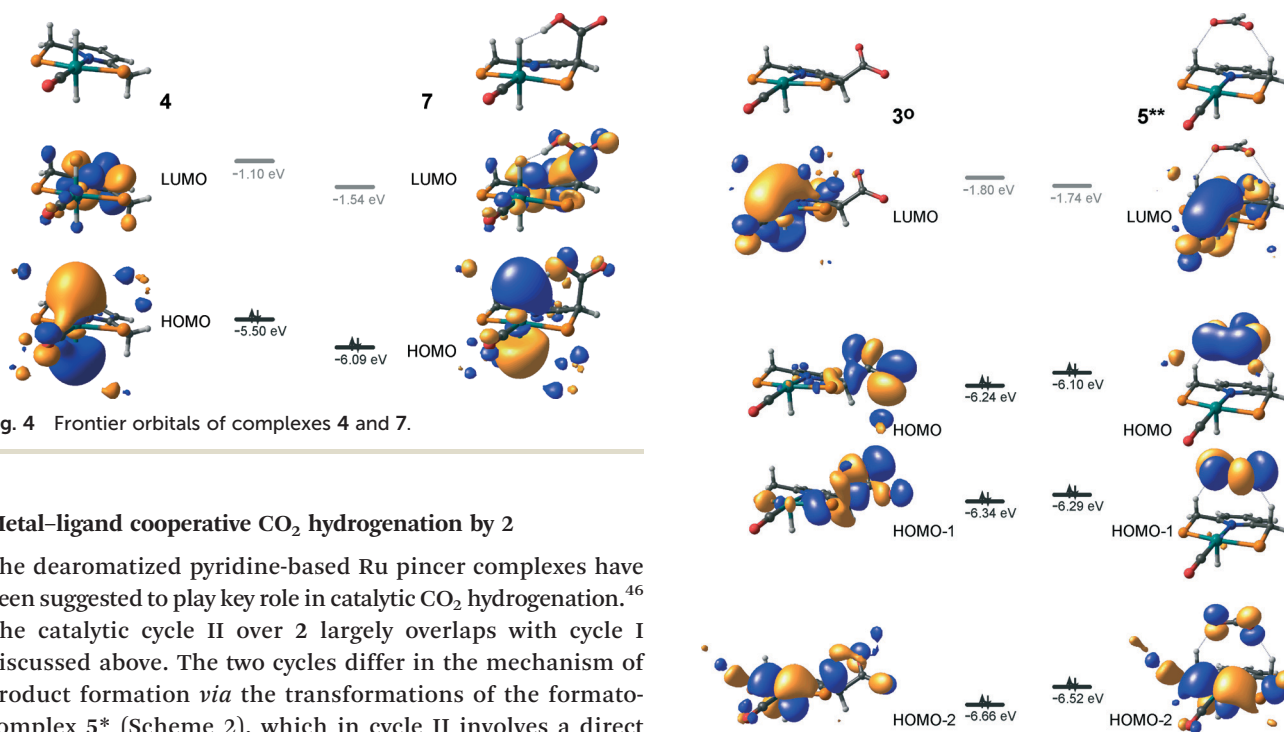


Fig. 4 Frontier orbitals of complexes **4** and **7**.

### Metal–ligand cooperative CO<sub>2</sub> hydrogenation by **2**

The dearomatized pyridine-based Ru pincer complexes have been suggested to play key role in catalytic CO<sub>2</sub> hydrogenation.<sup>46</sup> The catalytic cycle II over **2** largely overlaps with cycle I discussed above. The two cycles differ in the mechanism of product formation *via* the transformations of the formate-complex **5\*** (Scheme 2), which in cycle II involves a direct deprotonation of the PNP ligand resulting in a one-step FA formation. The DFT computed reaction energy diagram for CO<sub>2</sub> hydrogenation over **2** is shown in Fig. 6. Heterolytic dissociation of H<sub>2</sub> over **2** yielding **4** is the first and the most energy demanding step of the cycle ( $E^\ddagger = 76 \text{ kJ mol}^{-1}$ ). It is followed by a facile CO<sub>2</sub> activation by the bis-hydrido species **4** resulting in **5\***. The weakly bound HCOO<sup>-</sup> in **5\*** plays then a role of a base that attacks the acidic CH<sub>2</sub> moiety at the PNP pincer arm resulting in its deprotonation and the

Fig. 5 Frontier orbitals of complexes **30** and **5\*\***.

formation of FA molecule hydrogen-bonded with a basic C1 site at Ru-PNP\* (**2-FA**). The reaction and activation energies are very similar for this step ( $\Delta E_{\text{ZPE}} = 46 \text{ kJ mol}^{-1}$  and  $E^\ddagger = 47 \text{ kJ mol}^{-1}$ ). Because of the very high basicity of the deprotonated pincer arm in **2**, the reverse FA dissociation reaction is effectively barrierless. Therefore, to promote the



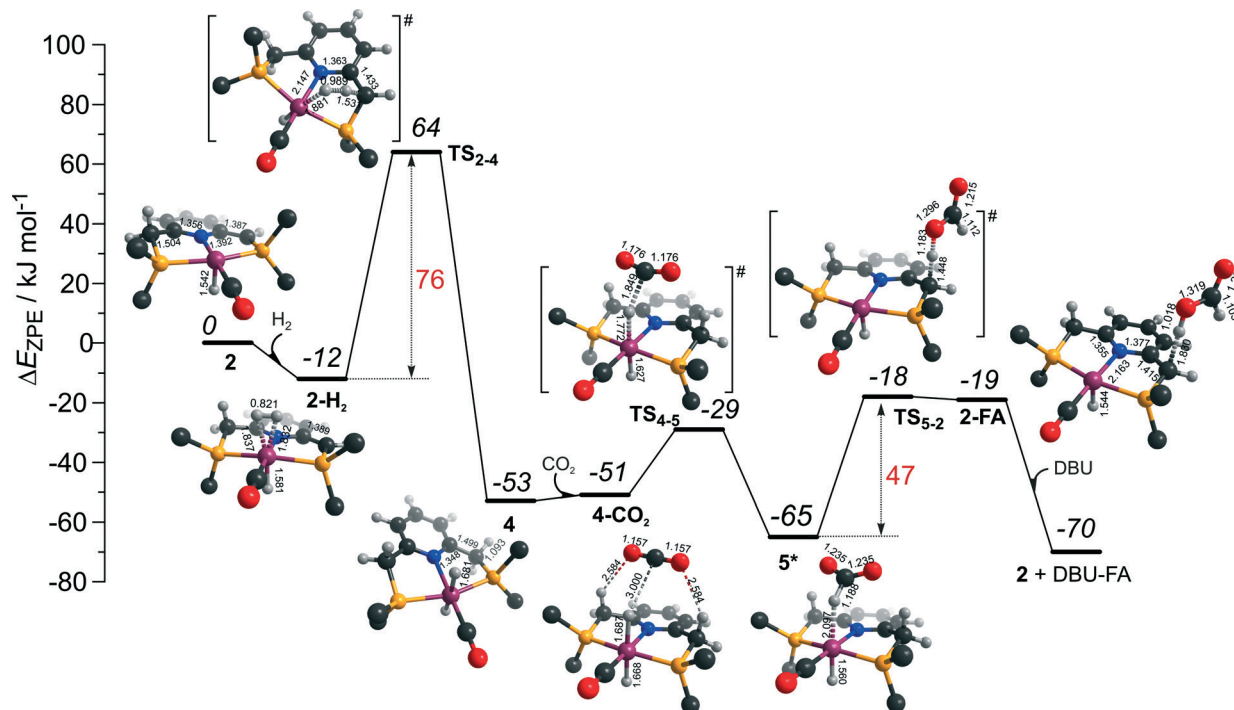


Fig. 6 DFT computed reaction energy diagram and optimized structures of the intermediate and transition states (CH<sub>3</sub> groups at the <sup>t</sup>Bu substituents of the PNP ligand are omitted for clarity) for the direct hydrogenation of CO<sub>2</sub> over 2 (cycle II).<sup>47</sup>

catalytic cycle FA has to be eliminated from the complex by a strongly exothermic ( $\Delta E_{ZPE} = -51 \text{ kJ mol}^{-1}$ ) reaction with DBU base. The DBU-FA product is formed at this step and the original catalytic species 2 is regenerated.

### CO<sub>2</sub> hydrogenation by 3

Potentially, the CO<sub>2</sub> adduct 3 can also act as catalytic species for CO<sub>2</sub> hydrogenation. In a very recent study by Huff and Sanford on the mechanism of CO<sub>2</sub> hydrogenation by a related Ru-PNN catalyst, the role of an Ru-PNN CO<sub>2</sub> adduct analogous to 3 has been discussed.<sup>46</sup> Although the mechanism for the catalytic reaction over such species was proposed, the authors concluded that it most likely represents a minor pathway in the overall catalytic process. The catalytic activity of the CO<sub>2</sub> adduct at elevated temperatures predominantly stems from the reversible binding of CO<sub>2</sub> that allows its transformations to a more reactive dearomatized Ru-PNN\* complex under the catalytic conditions. Similarly, in the presence of H<sub>2</sub> or H<sub>2</sub>-CO<sub>2</sub> mixture, 3 transforms directly to 5, from which cycle I<sup>3</sup> can in principle be initiated. The catalytic activities of these complexes are very different<sup>47</sup> suggesting the principle possibility of the 3-catalyzed hydrogenation of CO<sub>2</sub>.

The DFT-computed reaction energy diagram for the 3-catalyzed hydrogenation of CO<sub>2</sub> is shown in Fig. 7. To initiate the cycle III, complex 3 has to be activated *via* a rather unfavourable reaction ( $\Delta E = 33 \text{ kJ mol}^{-1}$ ,  $E^\ddagger = 69 \text{ kJ mol}^{-1}$ ) with H<sub>2</sub> that results in an opening of the Ru-O coordination and the formation of a 3°-H<sub>2</sub>. The coordinated dihydrogen molecule undergoes then a heterolytic dissociation over a cationic Ru center and the basic

carboxylate moiety on the pincer arm in 3°. The reaction in this case is less energetically favorable and proceeds with a higher barrier (3°-H<sub>2</sub> → TS<sub>3-7</sub> → 7,  $\Delta E = 9 \text{ kJ mol}^{-1}$ ,  $E^\ddagger = 15 \text{ kJ mol}^{-1}$ ) than the respective step in cycle I (5-H<sub>2</sub> → TS<sub>5-4</sub> → 4-FA,  $\Delta E = -9 \text{ kJ mol}^{-1}$ ,  $E^\ddagger = 2 \text{ kJ mol}^{-1}$ ). This is in line with the differences in energies of the frontier orbitals (Fig. 5) and, accordingly, the acid-base properties, of the reactive moieties in these complexes. Reaction of 7 with CO<sub>2</sub> yields a formato-complex 8 that resembles 5\* in cycle I. This step is slightly endothermic ( $\Delta E = 4 \text{ kJ mol}^{-1}$ ) and shows an activation barrier of 45 kJ mol<sup>-1</sup>. The lower reactivity of 7 towards CO<sub>2</sub> compared to that of catalyst 4 stems from the decreased hydricity of the Ru-H moiety interacting with the carboxylic acid group at the pincer arm of 7 (Fig. 4). Subsequent barrierless proton transfer from the ligand-bound -COOH moiety to the HCOO<sup>-</sup> anion in 8 results in FA hydrogen-bonded to the activated complex 3° (FA-3°). The removal of FA by the reaction with DBU regenerates the initial CO<sub>2</sub>-adduct 3.

### Implications for catalysis

The computational results presented above suggest that all candidate Ru-PNP complexes 2-4 can be formed under the CO<sub>2</sub> hydrogenation conditions and may contribute to the overall catalytic reaction. To directly compare the above three alternative mechanism for CO<sub>2</sub> hydrogenation by Ru-PNP, we further analysed reaction Gibbs free energy diagrams for these three catalytic cycles (Fig. 8).

The bis-hydrido complex 4 provides the lowest free energy reaction path for the conversion of CO<sub>2</sub> to FA-DBU along the cycle I (Fig. 8). The reaction in this case does not involve the



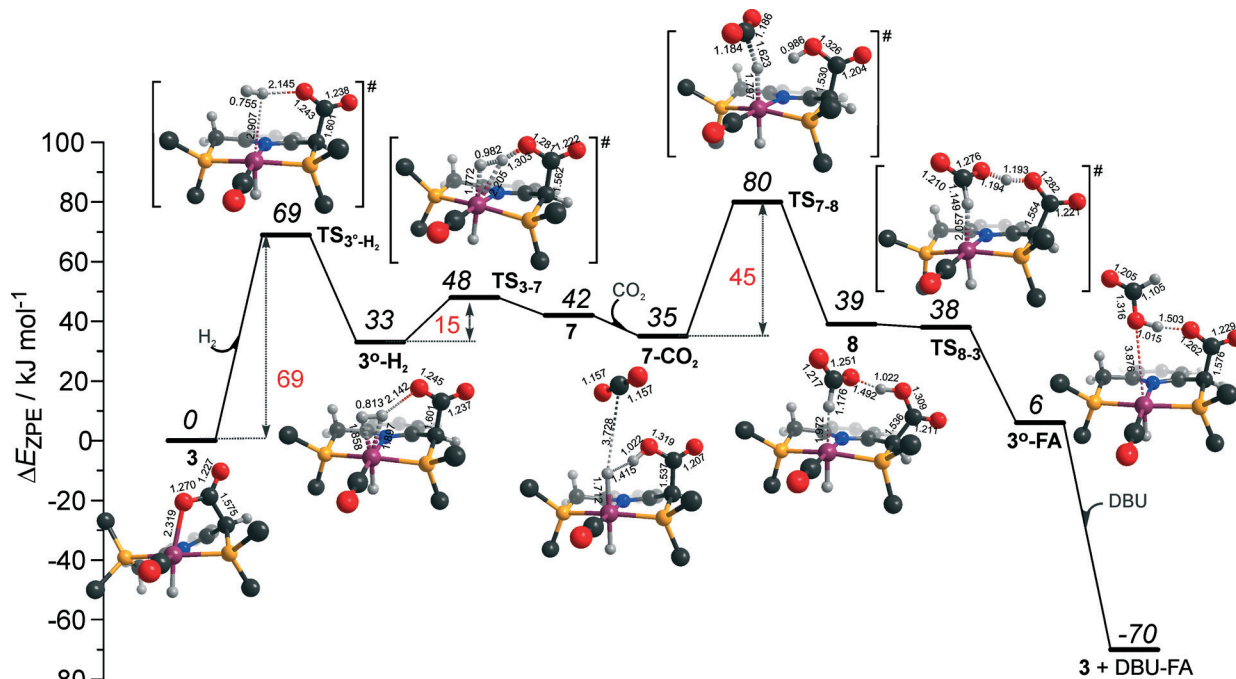


Fig. 7 DFT computed reaction energy diagram and optimized structures of the intermediate and transition states (CH<sub>3</sub> groups at the <sup>t</sup>Bu substituents of the PNP ligand are omitted for clarity) for the direct hydrogenation of CO<sub>2</sub> over **3** (cycle III).

metal–ligand cooperation in Ru-PNP and proceeds *via* the direct hydrogenolysis of transient species 5\* containing a non-coordinated formate anion (5\* + H<sub>2</sub> → 5-H<sub>2</sub> → 4-FA, Fig. 3 and 8). DFT calculations predict that the reaction along

this path shows a very low apparent activation energy<sup>68</sup> of 24 kJ mol<sup>-1</sup> (4 + CO<sub>2</sub> → 5\*, Fig. 3) associated with the initial CO<sub>2</sub> activation step. The free energy barrier  $\Delta G^\ddagger$  for this transformation is 67 kJ mol<sup>-1</sup> (Fig. 8). The subsequent facile

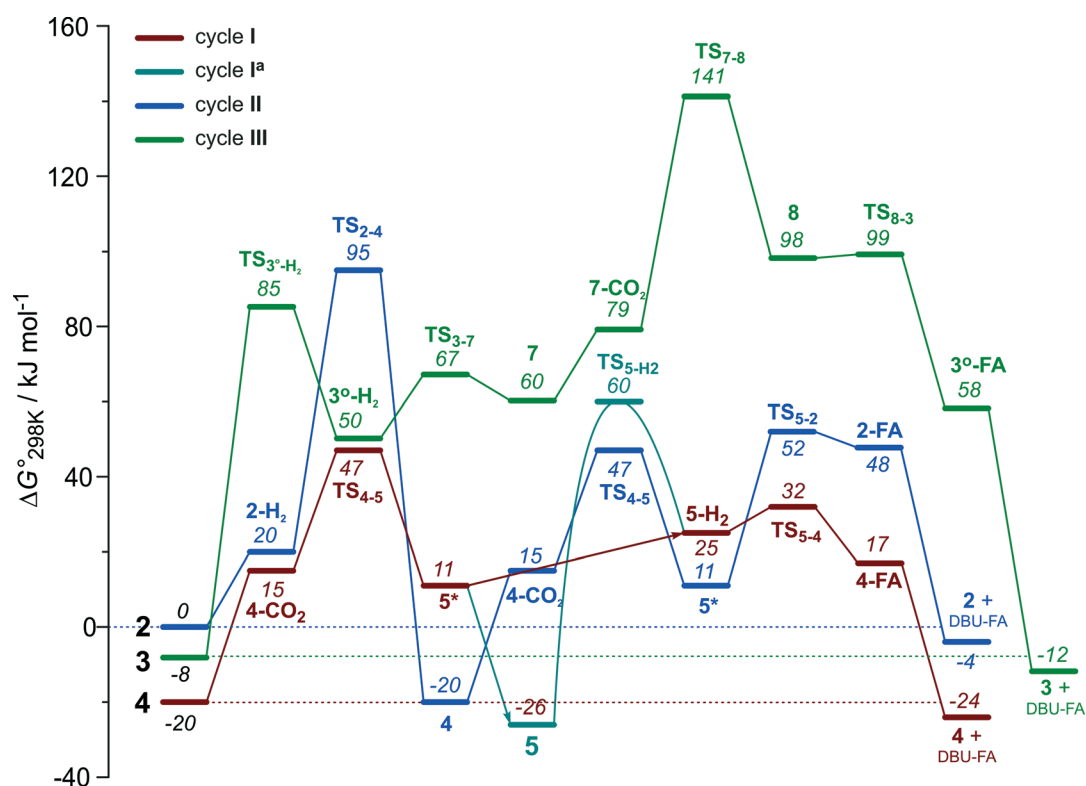


Fig. 8 A comparison of Gibbs free energy diagrams for catalytic cycles I, II and III plotted relative to the dearomatized Ru-PNP\* species **2**.





hydrogenolysis of  $5^*$  is competing with its rearrangement to a formate-complex  $5$ .  $5$  is the most thermodynamically stable species among the Ru-PNP intermediates considered here. This finding is in line with the results of experimental  $^1\text{H}$  NMR reactivity studies evidencing the exclusive formation of  $5$  under near-catalytic conditions.<sup>47</sup> The polarization of  $5$  followed by  $\text{H}_2$  insertion ( $5 + \text{H}_2 \rightarrow 5\text{-H}_2$ , Fig. 3) is the rate-determining step (RDS) of the catalytic mechanism involving the formation of  $5$  (cycle I<sup>a</sup>). This route is characterized by  $E_{\text{app}}^{\ddagger, \text{DFT}}$  of  $65 \text{ kJ mol}^{-1}$  that is comparable to the activation energies predicted for the elementary reaction steps involved in the alternative catalytic cycles II and III promoted by, respectively, complexes  $2$  and  $3$ .

The data in Fig. 6 and 8 suggest that the cooperative  $\text{H}_2$  activation by  $2$  represents the RDS of the MLC mechanism along the cycle II. Since the formation of an  $2\text{-H}_2$   $\sigma$ -complex is thermodynamically unfavourable, this route should proceed with a moderate  $E_{\text{app}}^{\ddagger, \text{DFT}}$  of  $64 \text{ kJ mol}^{-1}$  ( $2 + \text{H}_2 \rightarrow 4$ , Fig. 6). In free energy terms this pathway shows a rather high free energy barrier of  $95 \text{ kJ mol}^{-1}$  ( $2 + \text{H}_2 \rightarrow 4$ , Fig. 8). The catalysis on the  $\text{CO}_2$  adduct  $3$  (cycle III) proceeds *via* a sequence of thermodynamically unfavourable steps (Fig. 8). Although the initial coordination of  $\text{H}_2$  ( $3 + \text{H}_2 \rightarrow 3^{\circ}\text{-H}_2$ , Fig. 7) shows an activation energy ( $E^{\ddagger}$ ) of only  $69 \text{ kJ mol}^{-1}$ , the overall barrier in this case is represented by the energy difference between the initial state  $3$  and the high energy  $\text{TS}_{7-8}$  for the  $\text{CO}_2$  activation ( $E_{\text{app}}^{\ddagger, \text{DFT}} = 80 \text{ kJ mol}^{-1}$  Fig. 7,  $\Delta G_{\text{app}}^{\ddagger, \text{DFT}} = 149 \text{ kJ mol}^{-1}$  Fig. 8). In line with the experimental findings,<sup>47</sup> this points to a lower catalytic activity of  $3$  compared to that of  $2$  and  $4$ . Under the catalytic conditions, the contribution of  $2$  is limited due to the low thermodynamic stability of the reaction intermediates and high activation free energy barriers along the respective MLC path II.

Catalytic  $\text{CO}_2$  hydrogenation experiments with Ru-PNP catalyst precursor  $1$  and a strong  $\text{KO}^t\text{Bu}$  support this proposition. We propose that  $\text{KO}^t\text{Bu}$  can promote the dearomatization of the PNP pincer ligand<sup>60</sup> in the stable intermediates formed in the course of the reaction towards Ru-PNP\* complex  $2$  and therefore ensure the high steady-state concentration of this activated complex under the catalytic conditions. Independent of the reaction medium, a very low activity was observed in this case. Turnover numbers after 2 hour reaction (TON(2 h)) were only 728 and 649 in THF and DMF solvents, respectively. On contrary, when a non-nucleophilic DBU base, which cannot promote the ligand dearomatization,<sup>47</sup> was used as a promoter, much higher TON(2 h) values of 12 829 and 38 642 in THF and DMF solvents, respectively, were obtained (Table S1, ESI<sup>†</sup>).

The catalytic  $\text{CO}_2$  hydrogenation by Ru-PNP complexes is dominated by the competing reaction paths I and I<sup>a</sup> realized by the bis-hydrido Ru-PNP complex  $4$ . These paths are differentiated by the mechanism of the transformation of the polarized formate complex  $5^*$ . The competing rearrangement ( $5^* \rightarrow 5$ , path I<sup>a</sup>) and hydrogenolysis ( $5^* + \text{H}_2 + \text{DBU} \rightarrow 4 + \text{FA-DBU}$ , path I) routes show similar reaction free energy changes (Fig. 8) and involve effectively barrierless transformations (Fig. 3). We therefore speculate that the latter mechanism can

be promoted in the presence of an excess  $\text{H}_2$  that would ensure the rapid substitution of the non-coordinated  $\text{HCOO}^-$  and its replacement with  $\text{H}_2$  towards  $5\text{-H}_2$ .

To verify this hypothesis, we investigated the kinetics of  $\text{CO}_2$  hydrogenation by Ru-PNP complex  $1$  (Fig. 9) in the presence of DBU with varying  $\text{H}_2/\text{CO}_2$  molar ratio ( $p_{\text{total}} = 40 \text{ bar}$ ). At a  $\text{H}_2/\text{CO}_2$  molar ratio of 3/1, the reaction showed an apparent activation energy ( $E_{\text{app}}^{\ddagger}$ ) of  $57 \text{ kJ mol}^{-1}$  that is in very good agreement with the computed value ( $E_{\text{app}}^{\ddagger, \text{DFT}}$ ) of  $65 \text{ kJ mol}^{-1}$  for cycle I<sup>a</sup> (Fig. 3).

The rate enhancement previously observed upon a slight increase of the partial pressure of  $\text{H}_2$  (ref. 22) is in line with the proposition on the rate-determining nature of the  $5 + \text{H}_2 \rightarrow 5\text{-H}_2$  step in this case. As a result of the high activation energy, a strong temperature dependency of the reaction rate is observed. Whereas the reaction at  $132 \text{ }^\circ\text{C}$  shows an initial turnover frequency (TOF) of  $1\,892\,000 \text{ h}^{-1}$ , the initial TOF at  $90 \text{ }^\circ\text{C}$  is only  $266\,000 \text{ h}^{-1}$ . When the reaction is carried out in the presence of a large excess of  $\text{H}_2$  ( $\text{H}_2/\text{CO}_2 = 37/3$ ), the apparent activation energy drops to only  $20 \text{ kJ mol}^{-1}$ , which is in perfect agreement with the value of  $24 \text{ kJ mol}^{-1}$  predicted for the direct hydrogenolysis path I (Fig. 3). At a temperature of  $129 \text{ }^\circ\text{C}$ , the reaction shows a TOF of  $1\,099\,000 \text{ h}^{-1}$ . In line with the proposal on the RDS nature of the  $\text{CO}_2$  activation step in cycle I, the lower reaction rate for a high temperature

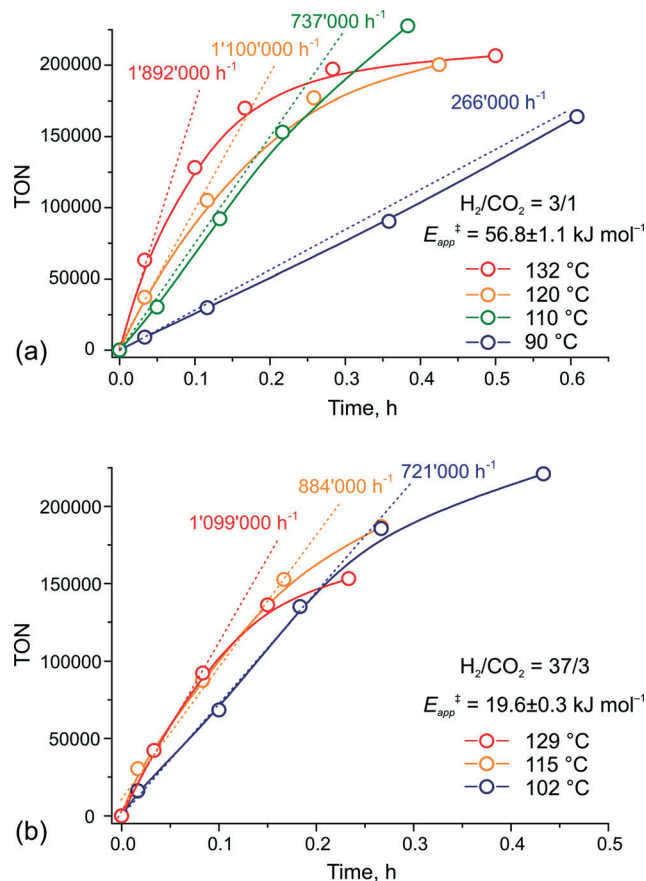


Fig. 9 Kinetic traces for  $\text{CO}_2$  hydrogenation by  $1$  at different temperatures and  $\text{H}_2\text{-CO}_2$  ratio of (a) 3/1 and (b) 37/3 ( $p_{\text{total}} = 40 \text{ bar}$ ).



reaction in this case is most likely due to the decreased partial pressure of CO<sub>2</sub>. An important consequence of the low activation barrier for CO<sub>2</sub> hydrogenation at a high H<sub>2</sub>/CO<sub>2</sub> molar ratio is the possibility to achieve high rates of the catalytic reaction at lower temperatures (Fig. 9(b)). An initial rate of 721 000 h<sup>-1</sup> was obtained at 102 °C. From the Arrhenius plot one can estimate TOF values above 100 000 h<sup>-1</sup> to be reachable at ambient temperature. These findings render the Ru-PNP complex **1** in combination with non-nucleophilic DBU base one of the most active CO<sub>2</sub> hydrogenation catalytic system reported to date.

## Conclusions

The mechanism of CO<sub>2</sub> hydrogenation to DBU formate salt in the presence of homogeneous pyridine-based Ru-PNP pincer catalysts was investigated by means of density functional theory calculations. The focus was on unravelling the complexity of the underlying reaction mechanisms and determining the routes for the optimization of the performance of this catalytic system. Dedicated catalytic tests and kinetic study were carried out to verify the theoretical predictions.

Three major interconnected reaction paths catalysed by dearomatised Ru-PNP\* complex **2** or by its cooperative adducts with CO<sub>2</sub> and H<sub>2</sub>, Ru-PNP complexes **3** and **4**, respectively, were considered. On the basis of the theoretical results it is proposed that depending on the reaction conditions, the relative concentration of these reactive species and their contribution to the overall catalytic performance varies. Whereas formation of **4** upon the reaction of **2** with H<sub>2</sub> is thermodynamically preferred, the competing [1,3]-CO<sub>2</sub> addition towards **3** is favoured kinetically. We propose that the latter route will dominate in excess strong base needed to ensure a high steady-state concentration of the activated precursor **2** and a high partial pressure of CO<sub>2</sub>. At increased H<sub>2</sub> partial pressure, the reaction will be driven towards the most stable dihydrido-Ru-PNP complex.

The hydrogenation of CO<sub>2</sub> catalysed by **3** proceeds *via* a sequence of highly endothermic elementary steps showing also rather high activation barriers. As a result, the highest apparent activation barrier of 80 kJ mol<sup>-1</sup> is predicted for the respective catalytic cycle III. This cycle is also characterized by a prohibitively high overall Gibbs free energy barrier of 149 kJ mol<sup>-1</sup>. In the case of the catalysis by the dearomatised species **2**, metal–ligand cooperation plays an important role in the reaction mechanism. The initial heterolytic H<sub>2</sub> dissociation over an acid–base pair formed by the 5-coordinated Ru centre and the deprotonated CH basic site at the PNP\* pincer arm is the rate-determining step ( $E_{\text{app}}^{\ddagger, \text{DFT}} = 64 \text{ kJ mol}^{-1}$ ,  $\Delta G_{\text{app}}^{\ddagger, \text{DFT}} = 95 \text{ kJ mol}^{-1}$ ). Despite the high intrinsic reactivity of the acid and base sites in Ru-PNP\*, their distant location within the rigid dearomatised pincer complex strongly hamper the heterolytic H<sub>2</sub> dissociation. When a much less basic HCOO<sup>-</sup> anion acts as the basic site in related steps over **3**<sup>o</sup> (cycle III) and **5**<sup>\*</sup> (cycle I) complexes, much lower activation barriers are predicted. Most of the reaction intermediates involved in the catalytic cycles II and III are rather unstable

thermodynamically and their transformations proceed with rather high free energy barriers. This suggests only minor contribution of these reaction paths under common CO<sub>2</sub> hydrogenation conditions.

DFT calculations predict that the bis-hydrido Ru-PNP complex **4** is the most active one. CO<sub>2</sub> hydrogenation by **4** can follow two mechanisms (cycle I and I<sup>a</sup>) that do not involve metal–ligand cooperative steps. A facile CO<sub>2</sub> activation by Ru–H moiety resulting in a non-coordinated HCOO<sup>-</sup> and a 5-coordinated cationic Ru-PNP (**5**<sup>\*</sup>) represents the initial step in both catalytic cycle. The cycles are distinguished by the mechanism of the subsequent transformations of **5**<sup>\*</sup> that, in turn, depends on the partial pressure of H<sub>2</sub>. Under excess H<sub>2</sub>, the substitution of the non-coordinated HCOO<sup>-</sup> anion in **5**<sup>\*</sup> with H<sub>2</sub> resulting in a  $\sigma$ -complex **5**–H<sub>2</sub> initiates an almost barrierless sequence of elementary steps towards the completion of the catalytic cycle and the formation of the FA–DBU product. The competing route I<sup>a</sup> involves the rearrangement of **5**<sup>\*</sup> towards a stable formato-complex **5** that has previously been proposed to be the resting state of the catalytic reaction. The polarization of **5** followed by H<sub>2</sub> insertion to yield **5**<sup>\*</sup> determines the overall reaction rate for the I<sup>a</sup> mechanism and shows an activation barrier of 65 kJ mol<sup>-1</sup>. The initial CO<sub>2</sub> activation is the rate-determining step in cycle I, for which an apparent activation energy of only 24 kJ mol<sup>-1</sup> is predicted.

The analysis of experimental reaction kinetics for CO<sub>2</sub> hydrogenation by Ru-PNP confirms these theoretical predictions. By increasing the molar H<sub>2</sub>–CO<sub>2</sub> ratio in the catalytic experiment from 3/1 to 37/3, the apparent activation energy decreases from 57 to 20 kJ mol<sup>-1</sup>, respectively, in a perfect agreement with the computed values. A relatively small temperature dependency of the reaction rate in the latter case points to the possibility of achieving very high catalytic performance in CO<sub>2</sub> hydrogenation by Ru-PNP under near-ambient temperatures.

## Acknowledgements

E.A.P. gratefully acknowledges the Technology Foundation STW and the Netherlands Organization for Scientific Research (NWO) for his personal VENI grant. SurfSARA and NWO are acknowledged for providing access to supercomputer resources (grant SH-231). The authors thank Dr. L. Leffort (DSM) for the possibility to carry out high-throughput experiments.

## Notes and references

- 1 M. Cokoja, C. Bruckmeier, B. Rieger, W. A. Herrmann and F. E. Kühn, *Angew. Chem., Int. Ed.*, 2011, **50**, 8510–8537.
- 2 K. Huang, C.-L. Sun and Z.-J. Shi, *Chem. Soc. Rev.*, 2011, **40**, 2435–2452.
- 3 T. Sakakura, J.-C. Choi and H. Yasuda, *Chem. Rev.*, 2007, **107**, 2365–2387.
- 4 C. Maeda, Y. Miyazaki and T. Ema, *Catal. Sci. Technol.*, 2014, **4**, 1482–1497.



- 5 C. J. Whiteoak, N. Kielland, V. Laserna, E. C. Escudero-Adán, E. Martin and A. W. Kleij, *J. Am. Chem. Soc.*, 2013, **135**, 1228–1231.
- 6 M. L. Lejkowski, R. Lindner, T. Kageyama, G. É. Bódizs, P. N. Plessow, I. B. Müller, A. Schäfer, F. Rominger, P. Hofmann, C. Futter, S. A. Schunk and M. Limbach, *Chem. – Eur. J.*, 2012, **18**, 14017–14025.
- 7 L. Zhang, J. Cheng, B. Carry and Z. Hou, *J. Am. Chem. Soc.*, 2012, **134**, 14314–14317.
- 8 B. Chatelet, L. Joucla, J.-P. Dutasta, A. Martinez, K. C. Szeto and V. Dufaud, *J. Am. Chem. Soc.*, 2013, **135**, 5348–5351.
- 9 T. Sakai, Y. Tsutsumi and T. Ema, *Green Chem.*, 2008, **10**, 337–341.
- 10 L. Wu, Q. Liu, I. Fleischer, R. Jackstell and M. Beller, *Nat. Commun.*, 2014, **5**, 3091.
- 11 C. Federsel, R. Jackstell and M. Beller, *Angew. Chem., Int. Ed.*, 2010, **49**, 6254–6257.
- 12 J. F. Hull, Y. Himeda, W.-H. Wang, B. Hashiguchi, R. Periana, D. J. Szalda, J. T. Muckerman and E. Fujita, *Nat. Chem.*, 2012, **4**, 383–388.
- 13 C. A. Huff and M. S. Sanford, *J. Am. Chem. Soc.*, 2011, **133**, 18122–18125.
- 14 S. Wesselbaum, T. vom Stein, J. Klankermayer and W. Leitner, *Angew. Chem., Int. Ed.*, 2012, **51**, 7499–7502.
- 15 Y.-N. Li, R. Ma, L.-N. He and Z.-F. Diao, *Catal. Sci. Technol.*, 2014, **4**, 1498–1512.
- 16 M. Nielsen, E. Alberico, W. Baumann, H.-J. Drexler, H. Junge, S. Gladiali and M. Beller, *Nature*, 2013, **495**, 85–89.
- 17 R. E. Rodríguez-Lugo, M. Trincado, M. Vogt, F. Tewes, G. Santiso-Quinones and H. Grützmacher, *Nat. Chem.*, 2013, **5**, 342–347.
- 18 F. Joó, *ChemSusChem*, 2008, **1**, 805–808.
- 19 S. Enthaler, *ChemSusChem*, 2008, **1**, 801–804.
- 20 A. Boddien, F. Gaertner, C. Federsel, P. Sponholz, D. Mellmann, R. Jackstell, H. Junge and M. Beller, *Angew. Chem., Int. Ed.*, 2011, **50**, 6411–6414.
- 21 C. Fellay, P. J. Dyson and G. Laurenczy, *Angew. Chem., Int. Ed.*, 2008, **47**, 3966–3968.
- 22 G. A. Filonenko, R. van Putten, E. N. Schulpen, E. J. M. Hensen and E. A. Pidko, *ChemCatChem*, 2014, **6**, 1526–1530.
- 23 A. Boddien, C. Federsel, P. Sponholz, D. Mellmann, R. Jackstell, H. Junge, G. Laurenczy and M. Beller, *Energy Environ. Sci.*, 2012, **5**, 8907–8911.
- 24 S.-F. Hsu, S. Rommel, P. Eversfield, K. Muller, E. Klemm, W. R. Thiel and B. Plietker, *Angew. Chem., Int. Ed.*, 2014, DOI: 10.1002/anie.201310972.
- 25 M. Drees, M. Cokoja and F. E. Kühn, *ChemCatChem*, 2012, **4**, 1703–1712.
- 26 T. Fan, X. Chen and Z. Lin, *Chem. Commun.*, 2012, **48**, 10808–10828.
- 27 C. Creutz, M. H. Chou, H. Hou and J. T. Muckerman, *Inorg. Chem.*, 2010, **49**, 9809–9822.
- 28 K.-W. Huang, J. H. Han, C. B. Musgrave and E. Fujita, *Organometallics*, 2006, **26**, 508–513.
- 29 T. Schaub and R. A. Paciello, *Angew. Chem., Int. Ed.*, 2011, **50**, 7278–7282.
- 30 C. Federsel, R. Jackstell and M. Beller, *Angew. Chem., Int. Ed.*, 2010, **49**, 6254–6257.
- 31 W. Wang, S. Wang, X. Ma and J. Gong, *Chem. Soc. Rev.*, 2011, **40**, 3703–3727.
- 32 R. Langer, Y. Diskin-Posner, G. Leitus, L. J. W. Shimon, Y. Ben-David and D. Milstein, *Angew. Chem., Int. Ed.*, 2011, **50**, 9948–9952.
- 33 C. Ziebart, C. Federsel, P. Anbarasan, R. Jackstell, W. Baumann, A. Spannenberg and M. Beller, *J. Am. Chem. Soc.*, 2012, **134**, 20701–20704.
- 34 M. S. Jeletic, M. T. Mock, A. M. Appel and J. C. Linehan, *J. Am. Chem. Soc.*, 2013, **135**, 11533–11536.
- 35 P. Munshi, A. D. Main, J. C. Linehan, C.-C. Tai and P. G. Jessop, *J. Am. Chem. Soc.*, 2002, **124**, 7963–7971.
- 36 Y.-Y. Ohnishi, T. Matsunaga, Y. Nakao, H. Sato and S. Sakaki, *J. Am. Chem. Soc.*, 2005, **127**, 4021–4032.
- 37 Y.-Y. Ohnishi, Y. Nakao, H. Sato and S. Sakaki, *Organometallics*, 2006, **25**, 3352–3363.
- 38 A. Urakawa, F. Jutz, G. Laurenczy and A. Baiker, *Chem. – Eur. J.*, 2007, **13**, 3886–3899.
- 39 R. Tanaka, M. Yamashita and K. Nozaki, *J. Am. Chem. Soc.*, 2009, **131**, 14168–14169.
- 40 C. Gunanathan and D. Milstein, *Acc. Chem. Res.*, 2011, **44**, 588–602.
- 41 J. I. van der Vlugt and J. N. H. Reek, *Angew. Chem., Int. Ed.*, 2009, **48**, 8832–8846.
- 42 E. Balaraman and D. Milstein, *Top. Organomet. Chem.*, 2014, **77**, 1–25.
- 43 R. Tanaka, M. Yamashita, L. W. Chung, K. Morokuma and K. Nozaki, *Organometallics*, 2011, **30**, 6742–6750.
- 44 X. Yang, *ACS Catal.*, 2011, **1**, 849–854.
- 45 M. S. G. Ahlquist, *J. Mol. Catal. A: Chem.*, 2010, **324**, 3–8.
- 46 C. A. Huff and M. S. Sanford, *ACS Catal.*, 2013, **3**, 2412–2416.
- 47 G. A. Filonenko, M. P. Conley, C. Copéret, M. Lutz, E. J. M. Hensen and E. A. Pidko, *ACS Catal.*, 2013, **3**, 2522–2526.
- 48 C. A. Huff, J. W. Kampf and M. S. Sanford, *Organometallics*, 2012, **31**, 4643–4645.
- 49 M. Vogt, M. Gargir, M. A. Iron, Y. Diskin-Posner, Y. Ben-David and D. Milstein, *Chem. – Eur. J.*, 2012, **18**, 9194–9197.
- 50 J. Zhang, G. Leitus, Y. Ben-David and D. Milstein, *Angew. Chem., Int. Ed.*, 2006, **45**, 1113–1115.
- 51 C. Adamo and V. Barone, *J. Chem. Phys.*, 1999, **110**, 6158–6170.
- 52 *Gaussian 09 Revision D.01*, M. J. Frisch, G. W. Trucks, H. B. Schlegel, G. E. Scuseria, M. A. Robb, J. R. Cheeseman, G. Scalmani, V. Barone, B. Mennucci, G. A. Petersson, H. Nakatsuji, M. Caricato, X. Li, H. P. Hratchian, A. F. Izmaylov, J. Bloino, G. Zheng, J. L. Sonnenberg, M. Hada, M. Ehara, K. Toyota, R. Fukuda, J. Hasegawa, M. Ishida, T. Nakajima, Y. Honda, O. Kitao, H. Nakai, T. Vreven, J. A. Montgomery Jr., J. E. Peralta, F. Ogliaro, M. Bearpark, J. J. Heyd, E. Brothers, K. N. Kudin,



- V. N. Staroverov, R. Kobayashi, J. Normand, K. Raghavachari, A. Rendell, J. C. Burant, S. S. Iyengar, J. Tomasi, M. Cossi, N. Rega, N. J. Millam, M. Klene, J. E. Knox, J. B. Cross, V. Bakken, C. Adamo, J. Jaramillo, R. Gomperts, R. E. Stratmann, O. Yazyev, A. J. Austin, R. Cammi, C. Pomelli, J. W. Ochterski, R. L. Martin, K. Morokuma, V. G. Zakrzewski, G. A. Voth, P. Salvador, J. J. Dannenberg, S. Dapprich, A. D. Daniels, Ö. Farkas, J. B. Foresman, J. V. Ortiz, J. Cioslowski and D. J. Fox, Gaussian, Inc., Wallingford CT, 2009.
- 53 Y. Zhao and D. G. Truhlar, *J. Chem. Theory Comput.*, 2009, 5, 324–333.
- 54 R. Valero, R. Costa, I. de P. R. Moreira, D. G. Truhlar and F. Illas, *J. Chem. Phys.*, 2008, 128, 114003.
- 55 R. Krishnan, J. S. Binkley, R. Seeger and J. A. Pople, *J. Chem. Phys.*, 1980, 72, 650–654.
- 56 A. D. McLean and G. S. Chandler, *J. Chem. Phys.*, 1980, 72, 5639–5648.
- 57 P. J. Hay and W. R. Wadt, *J. Chem. Phys.*, 1985, 82, 270–283.
- 58 P. J. Hay and W. R. Wadt, *J. Chem. Phys.*, 1985, 82, 299–310.
- 59 D. Andrae, U. Häußermann, M. Dolg, H. Stoll and H. Preuß, *Theor. Chim. Acta*, 1990, 77, 123–141.
- 60 B. Gnanaprakasam, J. Zhang and D. Milstein, *Angew. Chem., Int. Ed.*, 2010, 49, 1468–1471.
- 61 E. Khaskin, M. A. Iron, L. J. W. Shimon, J. Zhang and D. Milstein, *J. Am. Chem. Soc.*, 2010, 132, 8542–8543.
- 62 J. Kubas Gregory, *Acc. Chem. Res.*, 1988, 21, 120–128.
- 63 V. B. Kazansky and E. A. Pidko, *Catal. Today*, 2005, 110, 281–293.
- 64 R. H. Crabtree and M. Lavin, *J. Chem. Soc., Chem. Commun.*, 1985, 1661–1662.
- 65 R. H. Crabtree, *Acc. Chem. Res.*, 1990, 23, 95–101.
- 66 G. Alcaraz, M. Grellier and S. Sabo-Etienne, *Acc. Chem. Res.*, 2009, 42, 1640–1649.
- 67 M. Ahlquist, G. Fabrizi, S. Cacchi and P.-O. Norrby, *J. Am. Chem. Soc.*, 2006, 128, 12785–12793.
- 68  $E_{\text{app}}^{\ddagger, \text{DFT}}$  is defined as the difference in ZPE-corrected energy of the species corresponding to the highest and the lowest energy point in the reaction Gibbs free energy diagram for a particular proposed catalytic cycle (Fig. 8).

